Synthesis and characterization of copper antimony tin sulphide thin films for solar cell applications

N. Ali[1, 2]*, A. Hussain[1], R. Ahmed[1,], W N. Wan Shamsuri[1], Y.Q. Fu [3,]*****

[1]Department of Physics, Faculty of Science, Universiti Teknologi Malaysia, UTM Skudai, 81310 Johor, Malaysia
[2]Department of Physics, Govt. Post Graduate Jehanzeb College Saidu Sharif, Swat, 19200, Pakistan
[3]Department of Physics and Electrical Engineering, Faculty of Engineering & Environment, University of Northumbria, Newcastle upon Tyne, NE1 8ST, UK

Corresponding authors: *nisar.ali@utm.my (Nisar Ali); **rashidahmed@utm.my (R. Ahmed);

***richard.fu@northumbria.ac.uk (Richard Fu)

Abstract

Low-cost thin film modules based on copper antimony tin sulphide (CATS) were introduced for solar harvesting to compete for the already developed compound semiconductors. In this study, CATS thin films were deposited on soda lime glass using thermal evaporation technique followed by a rapid thermal annealing in an argon atmosphere. X-ray diffraction analysis revealed that the annealed samples were poly-crystalline and their crystallinity was improved with increasing annealing temperature. The constituent elements and their corresponding chemical states were identified using X-ray photoelectron spectroscopy. The obtained optical band gap for CATS thin film was found 1.58±0.06 eV which is nearly equal the optimal band gap value of CIGS and CdTe and GaAs - one of the highly efficient thin film material for solar cell technology. Furthermore, the good optical absorbance and low transmittance of the annealed CATS thin films in the visible region of light spectrum assured the suitability of the CATS thin films for solar cell applications.

Keywords: Thin films, Copper tin antimony sulphide, XPS, Optical properties, Resistivity

1. Introduction

Due to the rapid growth of population and extensive usage of electricity-consuming devices, the global use of energy is estimated to be as much as thirty terawatts by the year of 2050 [1-2]. The production of electricity from sustainable resources is vital to meet this great demand. One of the viable solutions is using thin-film solar cells, which are composed of different thin layers with various functions and tolerances for their optoelectronic properties on common substrates such as glass, polymer or silicon. Although various types of thin film materials are already commercially in use for photovoltaic (PV) applications, exploration of novel organic and inorganic thin film materials with an enhanced photovoltaic efficiency is greatly demanded [3-4]. The use of quantum dot and perovskite solar cell has also impacted the solar cell market in the last five years with the tremendous increase in their efficiency. In addition, combinatorial techniques have also been applied to obtain an appropriate elemental composition with different compounds [5-7].

Inorganic materials for solar cell technologies are of particular interest for commercialization because of their high efficiency, reliability and stability compared to those of the organic counterparts. To develop highly efficient and low cost inorganic solar cells, the metal-based chalcogenide materials have received considerable attention in the past two decades [8]. Among these, $CuInSe_2$, $CuInS_2$ (CIS), $AgInS_2$, $CuInGaS_2$ (CIGS), CdTe and Cu_2ZnSnS_4 (CZTS) have been extensively studied due to their high efficiency, ease of fabrication and superior optoelectronic properties [9]. However, the shortage of supplies of In, Ga, and toxicity of Se and Cd involved in the CIGS, CIS, CZTS, and CdTe are their intrinsic problems. Therefore, a considerable amount of research has been dedicated to searching the alternative materials [10-12]. In this regard, newly developed tin antimony sulphide (TAS) film has shown its potential for solar cell applications with its merits of abundance, nontoxic constituents and reasonably good performance [13-17]. Besides it has band gap energy from 2.5eV to 1.6eV for the annealed films, a high absorption coefficient (10^5 cm^{-1}) and superior photoconductivity values which are more appropriate for solar harvesting technology [18]. The inclusion of oxygen impurity in the TAS through annealing in oxygen environment was also reported to improve its PV module performance [19-21]. However, there are also issues associated with the TAS, such as its high

resistivity and n-type conductivity etc. [13]. The incorporation of copper in cadmium sulphide was also reported to change the conductivity type and increase the carrier mobility and carrier concentration [14-16].

In this work, we, for the first time as far as we know, explore a low-cost thin film of copper antimony tin sulphide (CATS) for application into thin film based photovoltaics. We report the influence of Cu content on the microstructure and Cu alloying in the CATS-based absorber layer [16]. Moreover, we investigate the post-annealing effects on its properties such as resistivity, grain growth and p-type conductivity for CATS thin films, in order to investigate its potential for solar cell applications.

2. Experimental

Powder of tin sulphide, antimony sulphide and copper sulphide (99.99% purity, Sigma-Aldrich) were used for thin films deposition. Soda lime glass substrate (2×2 cm^2) were rinsed ultrasonically by means of acetone/methanol, subsequently cleaning with deionized (DI) water and drying with nitrogen gas. A thin film of the CuSbSnS was deposited by co-evaporating mixed powders of tin sulphide, antimony sulphide and copper sulphide using a thermal evaporator (Edward model E-306). After doing so, the process of the post-annealing was carried out on the deposited thin films in a rapid thermal annealing equipment (ASO215R4-5782) for 20 minutes with different temperatures from 150^oC to 300^oC in pure Ar atmosphere. Film thickness of the deposited films was measured using a quartz crystal balance fitted inside the vacuum chamber and verified using scanning electron microscope. Surface and cross-section morphologies of the thin films were characterised using a field effect scanning electron microscope (FE-SEM, SU8020 X-Max^N Oxford with a 5 kV accelerating voltage). X-ray diffraction (XRD) measurements of the thin films were performed using a Siemens D500 diffractometer. The ultraviolet (UV)-visible-NIR (near infra-red) spectrometer (UV-3101PC) was used for optical analysis of the films. X-ray photoelectron spectroscopy (XPS) measurement was done via Kratos Axis Ultra X-ray photoelectron spectrometer with Al K_α radiation (1486.6 eV) source and, 240 μm spot size in the deposition chamber with a base vacuum of 4.0×10^{-9} Torr. The survey scans were recorded with a pass energy of 160eV, a step size of 1eV and a dwell time of 0.1 s, followed by a detailed scan of each element. To fit all the spectra, CasaXPS

software was used. The resistivity (ρ) and sheet resistance (Rs) of the film samples were measured using a Pro-4 four point probe together with a Keithley 2400 source-meter.

3. Results and discussion

XRD results of the as-deposited CATS thin films and those annealed at different temperatures are shown in **Fig. 1**. The as-deposited sample was found to be amorphous in nature, but with increasing annealing temperature the samples showed their polycrystalline structure. All the peaks identify polycrystalline nature of the $CuSbSnS_3$ with (1 1 0), (2 1 1), (1 1 1) and (2 0 0) diffractions planes. The crystallite size of the CATS thin films was estimated using the Debye-Scherrer's equation [22-23], based on the (2 0 0) peak:

$$D = \frac{0.9\lambda}{\beta\cos\theta} \quad (1)$$

where D is the crystallite size, λ is the wavelength of the x-rays used, β is the peak width at half maximum and θ is the diffraction Bragg's angle. The calculated crystallite sizes were about 15 ± 0.5, 17 ± 0.7, 17 ± 0.8 and 18 ± 0.9 nm for the samples annealed at 150, 200, 250 and 300°C respectively. It is clear from the XRD patterns that the intensity of the appeared peaks is increasing with increasing annealing temperature, and also the crystallite size of the annealed films increase with the annealing temperatures, as shown in the inset figure in Fig. 1.

The surface and cross-section morphology images of the as-deposited and 150 °C, 200 °C, 250 °C and 300 °C annealed samples are shown in **Fig. 2.** Clearly, densely distributed particulate structures are observed on the surface of the samples. The sample annealed at 150 °C and 200 °C **(see Fig. 2 (b-c))** contains agglomerated crystallites and irregular arrangements of crystallites on the surface of the film, indicating a poor crystallinity. With increasing annealing temperature to 300 °C, the crystallite sizes increase and become uniformly distributed as shown in **Fig. 2 (d-e)**, showing the enhancement of crystallinity and uniformity of the crystals. **Fig. 2 (e)** shows a densely packed microstructure of grains without apparent columnar morphology and appreciable voids observed at the glass-CATS thin film interface, indicating a good adhesion between the CATS thin film and glass substrate. The average thickness of the thin film calculated from the image **(Fig. 2f)** is ~ 500 ± 20 nm.

The chemical state analysis of the 200^0C annealed CATS thin film was obtained using XPS. Elements of Cu, Sb, Sn, and S are clearly identified from the typical survey spectrum as shown in **Fig. 3**. The high-resolution core level spectra of the identified elements are shown in **Figs. 4 (a-d)**, corresponding to Cu-2p, Sb-3d, Sn-3d, and S-2p, together with de-convoluted plots (dotted and dashed lines).

The magnified core level spectrum of Cu revealed a 2p doublet as shown in **Fig. 4 (a)**, at binding energies of 929.7 and 930.7 eV for Cu $2p_{3/2}$, and 949.5 and 950.3 eV for Cu $2p_{1/2}$, respectively, with a peak separation of 19.8 eV. The two Cu2p doublet peaks show similar chemical shifts indicating the formation of a single compound of copper [26-27]. The lower intense peaks at binding energies 930.7 and 950.3 eV are close to that of Cu_2S but we couldn't obtain this compound peaks from the XRD results, while the dominant peaks at the binding energies of 929.7 and 949.5 eV did not match those of any ternary compound according to the XPS database [25]. The concentration ratio of each peak to the main peak from lower to higher binding energies are 54.7%, 11.8%, 22.6% and 10.8% respectively, with the peak areas corrected using the relative sensitivity factor (RSF) are 4331, 935, 1793, and 857 as calculated from CasaXPS software. Accordingly, the ratio between the two peaks is estimated to be ~1:3, indicating the second peak binding is dominant on the film surface which probably corresponds to the CATS compound. **Fig. 4(b)** display high-resolution spectra for $Sb_{5/2}$ and $Sb_{3/2}$ core levels along with the de-convoluted plots. The main peaks of Sb are observed at binding energies 529.8 and 538.8 eV as marked in **Fig. 4 (b)**, revealing the existence of Sb^{3+} in Sb_2S_3 [28-29]. The entire component peaks were observed at binding energies of 527.5, 528.6, 529.8 and 531.0 eV for Sb $3d_{5/2}$ and 536.8, 537.8, 538.8 and 539.9 eV for Sb $3d_{3/2}$ corresponding to the elemental state of antimony [25]. The peaks observed at binding energies 527.5 and 536.8 eV are corresponding to the elemental state of antimony (Sb) and those observed at 528.6 and 537.8 eV to Sb^{3+} in stibnite [23]. The combined peak areas of the component peaks calculated with the RSF corrections starting from lower to higher binding energy values are 2574 for Sb and 5392 for Sb^{3+} and hence the ratio between them is approximated to be ~1:2. This indicates that Sb^{3+} is dominant on the surface of the CATS film.

The Sn 3d spectra in **Fig. 4 (c)** show two major peaks at binding energy values of 485.7 and 494.3 eV corresponding to $3d_{5/2}$ and $3d_{3/2}$ core levels along with the de-convoluted (dotted lines)

spectra at 483.7 485.3 and 486.4 eV for $3d_{5/2}$ and 492.7, 493.9 and 495.0 eV for $3d_{3/2}$ correspondingly. The peaks appeared at binding energy values of 483.7 and 492.7 eV correspond to the elemental state of Sn [24]. Similarly, the peaks observed at 485.3 and 493.9 eV are very close to the binding energy values of $SnMo_6S_8$ according to the database, with the peak areas of 8250 and 4490, respectively. Moreover, those peaks appeared at 486.4 and 495.0 eV having peak areas of 4326 and 3143, respectively, have not matched with any ternary or quaternary compounds in the database [24]. The percentage atomic concentrations of the component peaks are 13.1%, 32.2% and 16.8% for Sn $3d_{5/2}$ and 7.9%, 17.5% and 12.2% for Sn $3d_{3/2}$, indicating the ratio is about 1: 3: 2.

The S 2p core level and corresponding de-convoluted spectra (**Fig. 4 (d)**) show six distinct peaks at 158.8, 160.1, 161.1, 161.8, 162.2 and 162.4 eV binding energies. The values of the binding energies for S 2p are consistent with the range for S in sulphide phases [25-26]. The corresponding binding energy values for all the CATS elements are in full agreement with those in the literature [24-30]. Therefore, combining the results of the binding energy values from the XPS and the phases from the XRD we assign the studied phase to be $CuSbSnS_3$.

The optical absorbance and transmittance T (%) spectra of the as-deposited and annealed CATS samples at different annealing temperatures (150-300^{o}C) are shown in **Fig. 5 (a, b)** with the wavelength range from 300-1200 nm. The instrument was calibrated (baseline setting procedure) using a bare glass substrate as a reference for the absorbance and transmittance measurements. The transmittance spectra of the deposited films are the lowest and almost zero for the samples annealed at 250 and 300^{0}C in the visible region of the optical spectrum. In the region from 700-900 nm, an average transmittance of 30% was observed for the sample annealed at 300^{0}C, which is mainly attributed to the high absorption of antimony, i.e., nearly 50% absorption occurs in the region. A decrease in the transmittance (40 to 20%) at a wavelength of 500 to 1200 nm was observed with 300^{0}C annealing temperature which may be attributed to the structural changes of the samples with increasing annealing temperature. The value of the optical band gap of the thin films was estimated using a standard Tauc's Plot equation [31]:

$$(\alpha h\nu)^{n} = B\,(h\nu - E_g) \qquad (2)$$

where E_g is the optical band gap and n=2, 1/2, 3/2 for direct allowed, indirect allowed and direct forbidden transitions, respectively, α is the optical absorption coefficient at frequency ν and B is a constant. The absorption coefficient in the absorbing region can be determined using the following relation [13]:

$$\alpha = 2.303 \frac{A}{d} \quad (3)$$

where d is the thickness of the thin films (~500 nm), and A represents the absorbance of the samples. **Fig. 5 (c)** displayed the plot $(\alpha h\nu)^n$ vs. hν (Tauc plot) for the as grown CATS thin film and those annealed at different temperatures (150-300 °C), showing a good linear fit with n=2. The values of the respective optical band gaps for all the samples were estimated by extrapolating the linear region of the plot to α = 0, as displayed in Fig 5(c) and the possible errors in the values are displayed in Fig 5(d). The optical band gap values calculated from the graphs are in the range of 1.5 to 2.3 eV, with the film annealed at the highest temperature (300 °C) has the lowest E_g value (1.58 eV). This value is almost the optimum value for solar cell applications, similar to that of GaAs. Therefore the annealed CATS thin films could be an appropriate material for the absorber layer in solar cell applications.

Figs. 6(a) and 6(b) show a plot of electrical resistivity with errors and sheet resistance as functions of annealing temperature. A decrease in the resistivity of the samples is observed with increasing annealing temperature, which can be accredited to the improved quality of the grains and grain sizes of the annealed CATS thin films due to the decreased grain boundaries scattering and increase in carrier mobility. The plot of sheet resistance shown in **Fig. 6 (b)** confirmed the uniformity of the samples.

4. Conclusions

The CATS thin films were deposited on soda lime glass by thermal evaporation technique. The structural, electrical and optical properties of the fabricated samples were greatly influenced by post-annealing in argon gas atmosphere. The crystalline structure, component elements, and their chemical states were identified using X-ray diffraction and X-ray photoelectron spectroscopy. The results showed that crystallinity and uniformity of the samples were improved with increasing annealing temperature. High optical absorbance in the near ultraviolet and visible

light region and corresponding low transmittance of the post-annealed films in the visible light range, assured the suitability of the CATS thin films for solar cell applications. The optical band gap of the CATS thin films was found to be 1.58 eV, which is the optimum value for the absorber layer in solar cells, being a potential cheap but efficient material for solar cell technology.

Acknowledgement

The authors would like to thank University Teknologi Malaysia and Ministry of Education Malaysia for the financial support of this research work through project nos. Q.J130000.2526.10H77, R.J130000.7826.4F508, Q.J130000.2526.12H46, Post-Doctoral Fellowship Scheme under project no. Py/2014/03074 and International Doctoral Fellowship 176–BIASISWAZAH UTM IDF. Special thanks to Miss Siti Zahara Binti Salleh, University Laboratory Management Unit, UTM for providing XPS facility. Funding support from the UoA and CAPEX from Northumbria University at Newcastle and Royal academy of Engineering is acknowledged.

Reference

[1] S. Chu, A. Majumdar, Nature, 488 (2012) 294-303.

[2] M.G. Brik, M. Piasecki, I.V. Kityk, Inorganic Chemistry, 53 (2014) 2645-2651.

[3] M. Graetzel, R.A.J. Janssen, D.B. Mitzi, E.H. Sargent, Nature, 488 (2012) 304-312.

[4] Yandjah, L., et al., *Preparation and characterization of flash-evaporated CuInSe2/CuGaSe2 thin films.* Optical Materials, 2010. **32**(7): p. 772-775.

[5] Ali, N., et al., A novel approach for the synthesis of tin-antimony sulphide thin films for photovoltaic application. Solar Energy, 2015. 113: p. 25-33.

[6] Ali, N., et al., Advances in nanostructured thin film materials for solar cell applications. Renewable and Sustainable Energy Reviews, 2016. 59: p. 726-737.

[7] Zhao, D. and C.-F. Yang, Recent advances in the TiO2/CdS nanocomposite used for photocatalytic hydrogen production and quantum-dot-sensitized solar cells. Renewable and Sustainable Energy Reviews, 2016. 54: p. 1048-1059.

[8] M. Liu, M.B. Johnston, H.J. Snaith, Nature, advance online publication (2013).

[9] S. Lugo, I. López, Y. Peña, M. Calixto, T. Hernández, S. Messina, D. Avellaneda, Thin Solid Films, 569 (2014) 76-80.

[10] R. Touati, M.B. Rabeh, M. Kanzari, Energy Procedia, 44 (2014) 44-51.

[11] Gedi, S., et al. (2016). "A facile inexpensive route for SnS thin film solar cells with SnS2 buffer." Applied Surface Science **372**: 116-124.

[12] Zhou, D., et al. (2016). "Sputtered molybdenum thin films and the application in CIGS solar cells." Applied Surface Science **362**: 202-209.

[13] N. Ali, R. Ahmed, B. ul Haq, A. Shaari, M. Jabeen, Measurement, 63 (2015) 81-86.

[14] Cusano, D.A., CdTe solar cells and photovoltaic heterojunctions in II–VI compounds. Solid-State Electronics, 1963. **6**(3): p. 217-218.

[15] Shah, N.A., et al., Cu-doping effects on the physical properties of cadmium sulfide thin films. Journal of Alloys and Compounds, 2012. 512(1): p. 185-189.

[16] Caballero, R., et al., Cu deficiency in multi-stage co-evaporated Cu(In,Ga)Se2 for solar cells applications: Microstructure and Ga in-depth alloying. Acta Materialia, 2010. **58**(9): p. 3468-3476.

[17] A. Gassoumi, M. Kanzari, B. Rezig, The European Physical Journal - Applied Physics, 41 (2008) 91-95.

[18] C. Wang, C. Zhu, T. Zhang, Materials Letters, 108 (2013) 62-64.

[19] A. Gassoumi, M. Kanzari, Physica E: Low-dimensional Systems and Nanostructures, 44 (2011) 71-74.

[20] N. Ali, S.T. Hussain, Y. Khan, N. Ahmad, M.A. Iqbal, S.M. Abbas, Materials Letters, 100 (2013) 148-151.

[21] M. B. Rabeh, M. Kanzari and B. Rezig, Thin Solid Films **515** (15), 5943-5948 (2007).

[22] S.A. Vanalakar, G.L. Agawane, S.W. Shin, M.P. Suryawanshi, K.V. Gurav, K.S. Jeon, P.S. Patil, C.W. Jeong, J.Y. Kim, J.H. Kim, Journal of Alloys and Compounds, 619 (2015) 109-121.

[23] Ayachi, B., et al. (2016). "Rapid thermal annealing effect on the spatial resistivity distribution of AZO thin films deposited by pulsed-direct-current sputtering for solar cells applications." Applied Surface Science **366**: 53-58.

[24] Wagner, C. D. *Handbook of X-ray photoelectron spectroscopy*. Edited by G. E. Muilenberg. Perkin-Elmer, 1979.

[25] C.D. Wagner, A.V. Naumkin, A. Kraut-Vass, J.W. Allison, C.J. Powell, J.R.Jr. Rumble, NIST Standard Reference Database 20, Version 3.4 (web version) (http://srdata.nist.gov/xps/) 2003.

[26] Fan, John CC, and John B. Goodenough. "X-ray photoemission spectroscopy studies of Sn-doped indium-oxide films." *Journal of Applied Physics* 48, no. 8 (1977): 3524-3531.

[27] B. Ananthoju, F. J. Sonia, A. Kushwaha, D. Bahadur, N. Medhekar and M. Aslam, Electrochimica Acta **137**, 154-163 (2014).

[28] B. Pawar, S. Pawar, S. Shin, D. Choi, C. Park, S. Kolekar and J. Kim, Applied Surface Science **257** (5), 1786-1791 (2010).

[29] R. Ornelas-Acosta, S. Shaji, D. Avellaneda, G. Castillo, T. D. Roy and B. Krishnan, Materials Research Bulletin **61**, 215-225 (2015).

[30] B. Yang, L. Wang, J. Han, Y. Zhou, H. Song, S. Chen, J. Zhong, L. Lv, D. Niu and J. Tang, Chemistry of Materials **26** (10), 3135-3143 (2014).

[31] Garza, J. G., S. Shaji, A. C. Rodriguez, TK Das Roy, and B. Krishnan. "AgSbSe 2 and AgSb (S, Se) 2 thin films for photovoltaic applications." *Applied Surface Science* 257, no. 24 (2011): 10834-10838.

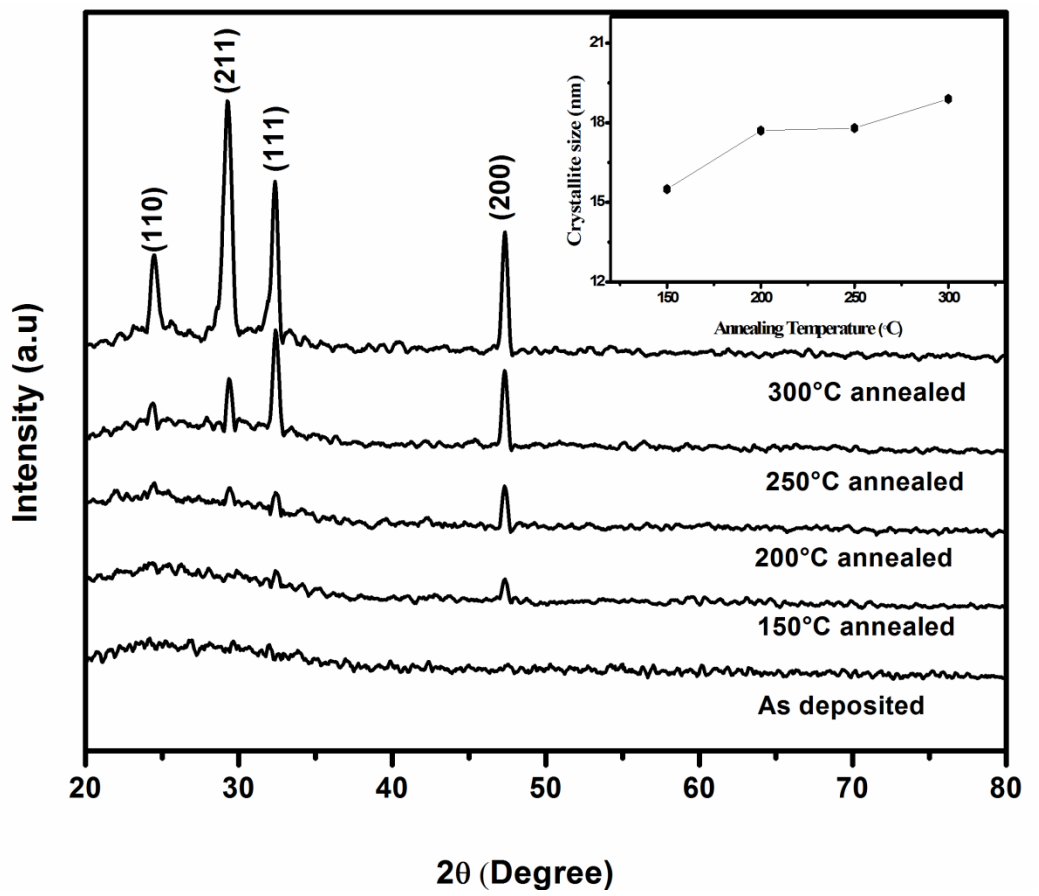

Fig. 1. XRD patterns of the as deposited and annealed CATS thin films with different temperatures in argon gas atmosphere; inet figure shows the calculated crystal sizes as a function of annealing temperature

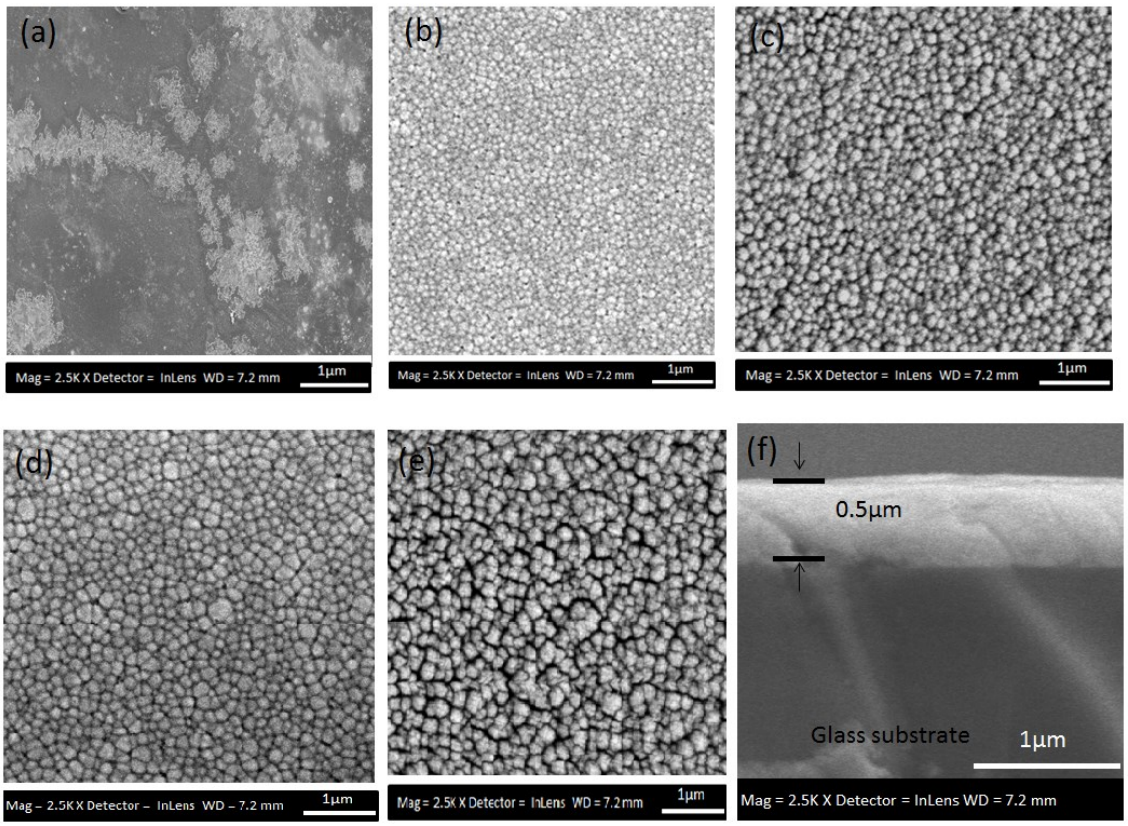

Fig. 2. FE-SEM images of CATS thin films (a) as deposited (b) 150 °C annealed film (c) 200 °C annealed film (d) 250 °C annealed film (e) 300 °C annealed film (f) cross sectional of 300 °C annealed film.

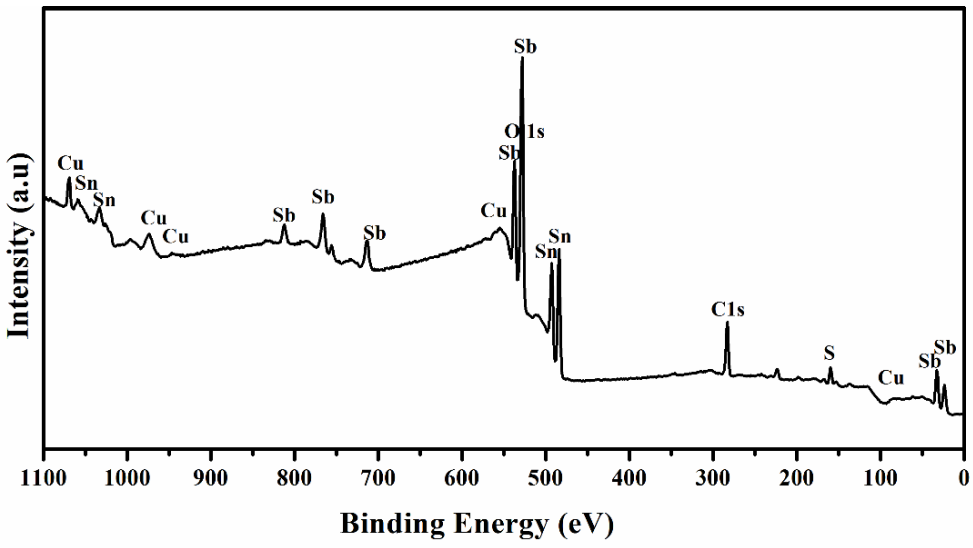

Fig. 3. XPS survey spectra of CATS thin film annealed at 200 °C in argon gas atmosphere.

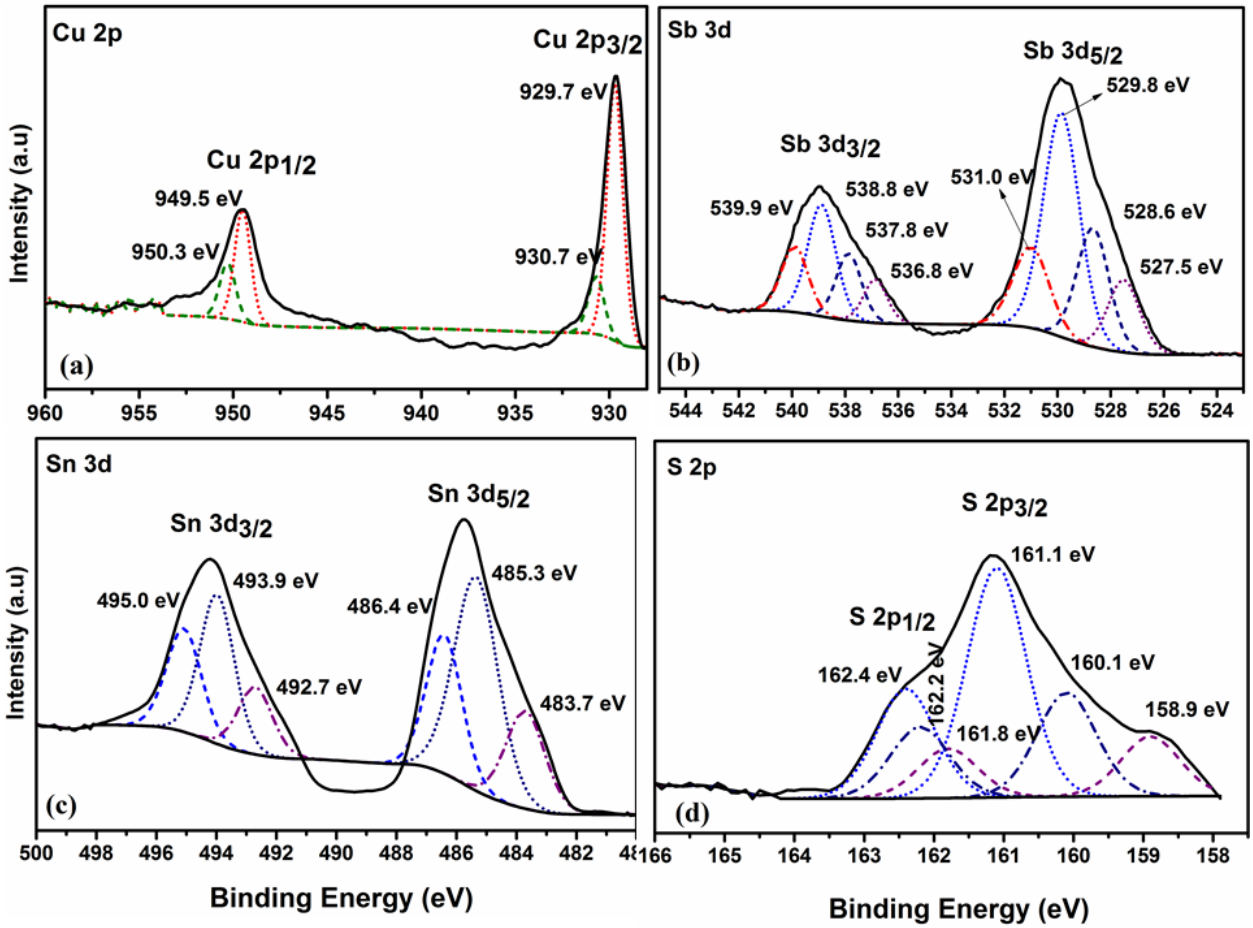

Fig. 4. High resolution spectra of (a) Cu 2p core level, (b) Sb 3d core level, (c) Sn 3d core level and (d) S 2p core level of CATS thin film annealed at 200 ^{0}C in argon atmosphere.

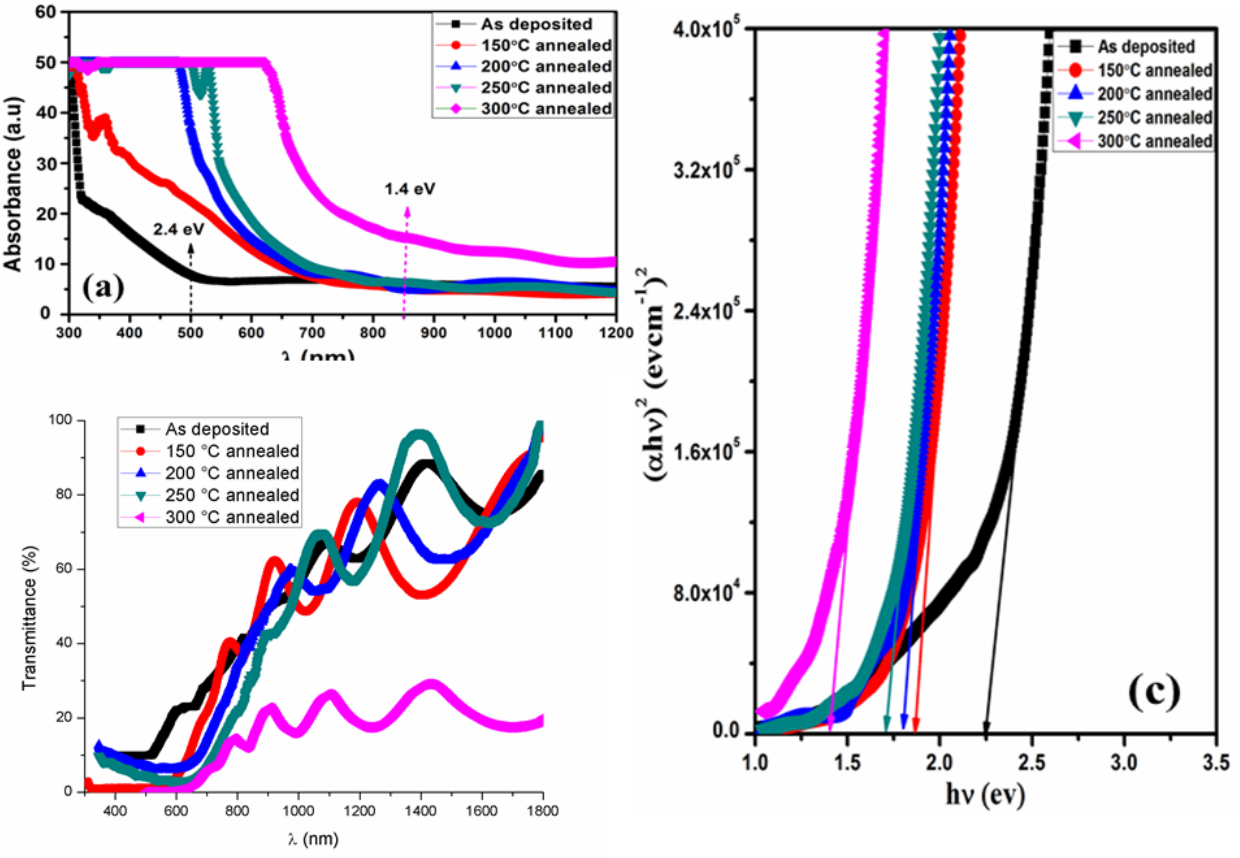

Fig. 5. Optical properties of the as deposited and annealed CATS thin films (a) Absorbance (b) Transmittance (c) Optical band gap (Tauc plot)

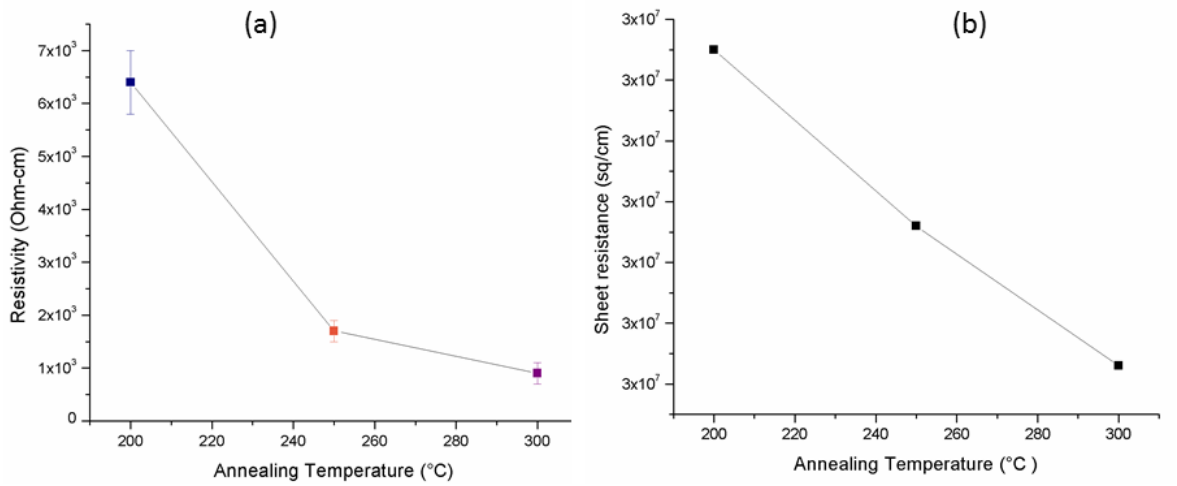

Fig. 6. Electrical properties of CATS thin films (a) Resistivity vs annealing temperature (b) Sheet resistance against annealing temperature.